

## Gyroaverage effects on chaotic transport by drift waves in zonal flows

Julio J. Martinell and Diego del-Castillo-Negrete

Citation: *Phys. Plasmas* **20**, 022303 (2013); doi: 10.1063/1.4790639

View online: <http://dx.doi.org/10.1063/1.4790639>

View Table of Contents: <http://pop.aip.org/resource/1/PHPAEN/v20/i2>

Published by the [American Institute of Physics](#).

---

### Related Articles

Suppression of drift wave turbulence and zonal flow formation by changing axial boundary conditions in a cylindrical magnetized plasma device

*Phys. Plasmas* **20**, 012304 (2013)

Electrostatic drift shocks and drift wave instability in inhomogeneous rotating electron-positron-ion plasmas

*Phys. Plasmas* **19**, 092102 (2012)

A link between nonlinear self-organization and dissipation in drift-wave turbulence

*Phys. Plasmas* **19**, 082318 (2012)

Drift and ion acoustic wave driven vortices with superthermal electrons

*Phys. Plasmas* **19**, 084503 (2012)

Suppression of drift waves in a linear magnetized plasma column

*Phys. Plasmas* **19**, 072102 (2012)

---

### Additional information on Phys. Plasmas

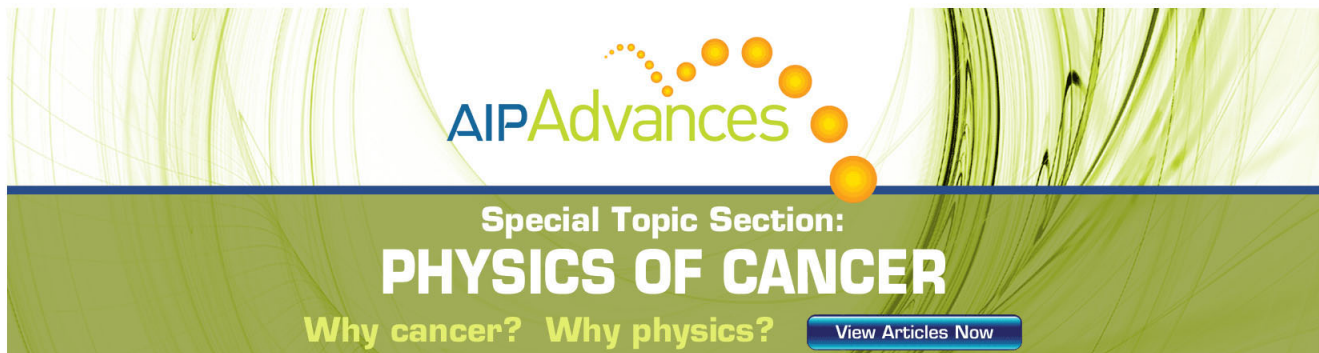
Journal Homepage: <http://pop.aip.org/>

Journal Information: [http://pop.aip.org/about/about\\_the\\_journal](http://pop.aip.org/about/about_the_journal)

Top downloads: [http://pop.aip.org/features/most\\_downloaded](http://pop.aip.org/features/most_downloaded)

Information for Authors: <http://pop.aip.org/authors>

## ADVERTISEMENT



**AIP Advances**

Special Topic Section:  
**PHYSICS OF CANCER**

Why cancer? Why physics? [View Articles Now](#)

## Gyroaverage effects on chaotic transport by drift waves in zonal flows

Julio J. Martinell<sup>1</sup> and Diego del-Castillo-Negrete<sup>2</sup>

<sup>1</sup>*Instituto de Ciencias Nucleares, Universidad Nacional Autónoma de México, Mexico D.F. 04510, Mexico*

<sup>2</sup>*Oak Ridge National Laboratory, Oak Ridge, Tennessee 37831, USA*

(Received 16 November 2012; accepted 10 January 2013; published online 8 February 2013)

Finite Larmor radius (FLR) effects on  $\mathbf{E} \times \mathbf{B}$  test particle chaotic transport in the presence of zonal flows is studied. The FLR effects are introduced by the gyro-average of a simplified  $\mathbf{E} \times \mathbf{B}$  guiding center model consisting of the linear superposition of a non-monotonic zonal flow and drift waves. Non-monotonic zonal flows play a critical role on transport because they exhibit robust barriers to chaotic transport in the region(s) where the shear vanishes. In addition, the non-monotonicity gives rise to nontrivial changes in the topology of the orbits of the  $\mathbf{E} \times \mathbf{B}$  Hamiltonian due to separatrix reconnection. The present study focuses on the role of FLR effects on these two signatures of non-monotonic zonal flows: shearless transport barriers and separatrix reconnection. It is shown that, as the Larmor radius increases, the effective zonal flow profile bifurcates and multiple shearless regions are created. As a result, the topology of the gyro-averaged Hamiltonian exhibits very complex separatrix reconnection bifurcations. It is also shown that FLR effects tend to reduce chaotic transport. In particular, the restoration of destroyed transport barriers is observed as the Larmor radius increases. A detailed numerical study is presented on the onset of global chaotic transport as function of the amplitude of the drift waves and the Larmor radius. For a given amplitude, the threshold for the destruction of the shearless transport barrier, as function of the Larmor radius, exhibits a fractal-like structure. The FLR effects on a thermal distribution of test particles are also studied. In particular, the fraction of confined particles with a Maxwellian distribution of gyroradii is computed, and an effective transport suppression is found for high enough temperatures. © 2013 American Institute of Physics. [<http://dx.doi.org/10.1063/1.4790639>]

### I. INTRODUCTION

Zonal shear flows are known to have a profound influence on transport in fluids and plasmas. Of particular interest is the relationship between the shear of the zonal flow and transport barriers. In the context of turbulent transport, it has been argued that an increase of shear can lead to a reduction of transport. This is because, under certain conditions, high enough flow shear can lead to reduction of the turbulence correlation length and thus to a decrease of the turbulent transport.<sup>1</sup> However, in the context of chaotic transport, the opposite is typically the case. In these systems, it has been observed that low levels of shear, and in particular, the presence of shearless regions is directly related to transport barriers.<sup>2–5</sup> It is interesting to point out that recent experimental studies reported in Ref. 6 indicate that transport in the Texas Helimak is not reduced in the high velocity shear regions.

In this paper we focus on the chaotic transport regime. That is, we assume that, from the Eulerian perspective, the system is not turbulent. However, because of deterministic chaos, there is Lagrangian turbulence, i.e., test particle trajectories exhibit sensitive dependence on initial conditions (positive Lyapunov exponents). As it is well-known, in the case of a constant, uniform magnetic field, the  $\mathbf{E} \times \mathbf{B}$  drift can be described by a Hamiltonian system with the electrostatic potential,  $\phi$ , playing the role of Hamiltonian and the perpendicular  $(x,y)$ -coordinates playing the role of canonically conjugate variables. When there is a reference frame in which  $\phi$  is time-independent, the Hamiltonian system is integrable and the isocontours of the potential define transport

barriers in the  $(x,y)$ -plane, also known as KAM (Kolmogorov-Arnold-Moser) curves. However, when perturbations with a time dependence that cannot be removed by a Galilean change of reference frame are added, the Hamiltonian system is in general not integrable. In this case, while some of the KAM curves are preserved others are destroyed and cease to act as transport barriers. The problem of the transition to chaos consists of determining when and how this happens. Lagrangian turbulence is relevant in systems dominated by coherent structures and in particular in systems with strong zonal shear flows.

Most of the previous works on chaotic transport have neglected finite Larmor radius effects. That is, in those studies, the passive tracers were advected using the guiding center  $\mathbf{E} \times \mathbf{B}$  Hamiltonian. Although this approximation is widely used, it fails when the Larmor radius is large, as it is the case, for example, for high energy  $\alpha$ -particles produced in fusion reactions. Among the few previous works on FLR effects on  $\mathbf{E} \times \mathbf{B}$  chaotic transport are Refs. 7 and 8. Reference 7 studied FLR effects on nondiffusive transport following a Lagrangian statistics approach. The Lagrangian velocity autocorrelation function and the statistical moments of particle displacements were shown to exhibit non-diffusive scaling due to Lévy flights induced by the zonal flow. The shape and the spatio-temporal self-similar anomalous scaling of the probability density functions of particle displacements were reproduced accurately by a non-local (in space and time) effective transport model. More recently, Ref. 8 showed that FLR effects give rise to a bifurcation of non-monotonic zonal flows that create multiple shearless

regions. This reference also presented a study of the dependence of the phase space topology and separatrix reconnection on the Larmor radius. Following Refs. 7 and 8, our study of FLR effects is based on the gyroaveraging<sup>9</sup> of the Hamiltonian model of chaotic transport by drift waves proposed in Ref. 4. FLR effects on turbulent transport, in general and in particular, sub-diffusive radial transport in Hasegawa-Wakatani turbulence with zonal flows have also been studied in Refs. 10–12.

Going beyond these previous studies, in the present paper, we focus on chaotic transport in non-monotonic zonal flows. We show that an increase of the Larmor radius leads to a bifurcation of the zonal flow profile that results in the formation of additional shearless curves and the improvement of confinement. We present necessary and sufficient conditions for this bifurcation to happen in the case of symmetric zonal flows and study its role in the phase space topology of the gyro-averaged Hamiltonian. We provide numerical evidence of the role of FLR on the reduction of chaotic transport. In particular, we show that FLR effects generically suppress chaos and can lead to the restoration of broken transport barriers. This result is of direct relevance to fusion plasmas as it implies better confinement for particles with large Larmor radii, e.g., thermonuclear  $\alpha$ -particles in burning plasmas. We present a detailed numerical study of the threshold for chaotic transport. We show that in the drift-wave amplitude versus Larmor radius plane, the boundary defining the threshold for the transition to global transport has a fractal-like structure. To explore the dependence of these results on the plasma temperature, we study the fraction of confined particles with a Maxwellian distribution of Larmor radii and find an effective suppression of chaotic transport for high-enough temperatures.

The rest of the paper is organized as follows. Section II defines the transport model. The starting point is the  $\mathbf{E} \times \mathbf{B}$  guiding center velocity with an electrostatic potential consisting of the superposition of two drift waves and a background zonal flow. The FLR model is then obtained from the gyro-average of the  $\mathbf{E} \times \mathbf{B}$  Hamiltonian. In Sec. III, we study the bifurcation of the zonal flow profile as function of the Larmor radius and the phase space topology of the gyro-averaged Hamiltonian in the integrable case with a single mode perturbation. Section IV presents a numerical study of the transition to chaos due to the destruction of transport barriers as function of the Larmor radius. It is shown that, for high enough mode amplitudes where transport barriers are no longer present when  $\rho = 0$ , a transport barrier can reappear as  $\rho$  increases from zero. The threshold for barrier destruction as function of the mode amplitude and the Larmor radius is determined. In Sec. V, we consider cross-flux transport for a thermal distribution of particles, corresponding to a Maxwellian distribution in  $\rho$ . The effectiveness of the transport barrier is measured by the fraction of total particles that cross the barrier. Section VI presents the summary and conclusions.

## II. FLR TEST PARTICLE TRANSPORT MODEL

We assume a slab model for a toroidal plasma with the  $(x, y, z)$  coordinates corresponding to the radial, poloidal, and

toroidal directions, respectively. The plasma density gradient is assumed along the  $x$ -coordinate and the magnetic field is constant and purely toroidal,  $\mathbf{B} = B\hat{z}$ . We limit attention to test particles, i.e., self-consistency effects are neglected and the particles are transported by the flow without modifying it. Only motion in the plane perpendicular to the magnetic field is considered so the model is two-dimensional. As mentioned before, when finite Larmor radius (FLR) effects are neglected, in the  $\mathbf{E} \times \mathbf{B}$  approximation the particle orbits are determined by

$$\frac{d\mathbf{r}}{dt} = \frac{\mathbf{E} \times \mathbf{B}}{B^2}, \quad (1)$$

where  $\mathbf{r} = (x, y)$  denotes the particle position and  $\mathbf{E}$  is the electrostatic field. Writing  $\mathbf{E} = -\nabla\phi(x, y, t)$ , Eq. (1) can be equivalently written as the Hamiltonian dynamical system

$$\frac{dx}{dt} = -\frac{\partial\phi}{\partial y}, \quad \frac{dy}{dt} = \frac{\partial\phi}{\partial x}, \quad (2)$$

where the electrostatic potential is the Hamiltonian, the spatial coordinates are the canonical conjugate phase space variables, and time has been rescaled by  $B$ .

The spatio-temporal dependence of the electrostatic potential of the drift-waves,  $\phi$ , is determined by the Hasegawa-Mima equation<sup>13</sup>

$$[\partial_t + (\mathbf{z} \times \nabla\phi) \cdot \nabla] (\nabla^2\phi - \phi - \beta x) = 0, \quad (3)$$

where the parameter  $\beta = n_0(x)/n_0(x)$  is the scale length of the density gradient. However, rather than solving this nonlinear drift equation, we follow Refs. 4, 14, and 15, and construct  $\phi$  using the eigenmodes of Eq. (3), i.e., we write

$$\phi = \varphi_0(x) + \sum_{j=1}^N \varepsilon_j \varphi_j(x) \cos k_j(y - c_j t), \quad (4)$$

where the first term on the right hand side of Eq. (4) corresponds to an equilibrium zonal shear flow,  $\mathbf{u}_0 = u_0(x) \mathbf{e}_y = \mathbf{e}_z \times \nabla\varphi_0$ , which will be taken to be a non-monotonic zonal flow of the form,

$$u_0(x) = U + \text{sech}^2 x, \quad (5)$$

and the second term on the right hand side of Eq. (4) is a superposition of linear drift waves with eigenfunctions  $\varphi_j$ , wave numbers,  $k_j$ , and wave velocities  $c_j$ . The variables are normalized to the characteristic length,  $L$ , and velocity,  $V$  of the zonal flow. Following Ref. 4, we use as eigenfunctions the two regular neutral modes of the system and write

$$\begin{aligned} \phi = & \tanh x - \eta x + \varepsilon_1 \text{sech}^2 x \cos(k_1 y) \\ & + \varepsilon_2 \text{sech}^2 x \cos(k_2 y - \omega t), \end{aligned} \quad (6)$$

where  $\eta = c_1 - U$ .

For relatively high energy particles, or for a flow varying relatively rapidly in space, the zero Larmor radius approximation fails and it is necessary to incorporate FLR effects. A simple, natural way of doing this is to substitute

the  $\mathbf{E} \times \mathbf{B}$  flow on the right hand side of Eq. (2), which is evaluated at the location of the guiding center, by its value averaged over a ring of radius  $\rho$ , where  $\rho$  is the Larmor radius.<sup>9</sup> Formally, the procedure is given by

$$\frac{dx}{dt} = -\left\langle \frac{\partial \phi}{\partial y} \right\rangle_{\theta}, \quad \frac{dy}{dt} = \left\langle \frac{\partial \phi}{\partial x} \right\rangle_{\theta}, \quad (7)$$

where the gyroaverage,  $\langle \cdot \rangle_{\theta}$ , is defined as

$$\langle \Psi \rangle_{\theta} \equiv \frac{1}{2\pi} \int_0^{2\pi} \Psi(x + \rho \cos \theta, y + \rho \sin \theta) d\theta. \quad (8)$$

This is a good approximation provided the gyrofrequency,  $\Omega_c$ , is greater than other frequencies in the system. Note that, as mentioned before, all the spatial scales have been non-dimensionalized using as length scale the characteristic width of zonal flow,  $L$ . Accordingly,  $\rho = \hat{\rho}/L$  where  $\hat{\rho}$  is the dimensional Larmor radius. In our two-mode model, this means  $\Omega_c \gg \omega$ . According to Eqs. (6) and (8), the gyro-averaged Hamiltonian is

$$\langle \phi \rangle_{\theta} = L_{0\rho}(x) - \eta x + \varepsilon_1 L'_{k_1\rho}(x) \cos(k_1 y) + \varepsilon_2 L'_{k_2\rho}(x) \cos(k_2 y - \omega t), \quad (9)$$

where the prime denotes the derivative and the function  $L_{k\rho}(x)$  defined by

$$L_{k\rho}(x) = \frac{1}{\pi} \int_0^{\pi} \tanh(x + \rho \cos \theta) \cos(k\rho \sin \theta) d\theta, \quad (10)$$

has the symmetries

$$L_{k\rho}(x) = -L_{k\rho}(-x), \quad L'_{k\rho}(x) = L'_{k\rho}(-x), \\ L''_{k\rho}(x) = -L''_{k\rho}(-x). \quad (11)$$

Substituting Eq. (9) into Eq. (7), we get the FLR test particles transport model

$$\frac{dx}{dt} = \varepsilon_1 k_1 L'_{k_1\rho}(x) \sin k_1 y + \varepsilon_2 k_2 L'_{k_2\rho}(x) \sin(k_2 y - \omega t), \quad (12)$$

$$\frac{dy}{dt} = L'_{0\rho}(x) - \eta + \varepsilon_1 L''_{k_1\rho}(x) \cos k_1 y + \varepsilon_2 L''_{k_2\rho}(x) \cos(k_2 y - \omega t). \quad (13)$$

Gyro-averaged calculations are time consuming because they require a 2-dimensional ring-averaged of the  $\mathbf{E} \times \mathbf{B}$  guiding center velocity field. However, in the proposed model, the relative simplicity of the gyro-averaged Hamiltonian reduces the computation to the evaluation of the 1-dimensional average defining the function  $L_{k\rho}(x)$  in Eq. (10). Depending on the problem and the computational resources, the 1-dimensional averages can be computed every time they are needed for the integration of the orbits, or else the functions  $L_{k\rho}(x)$  can be computed before-hand and interpolated at each integration step. Another option is to resort to analytical approximations of Eq. (10). For example, in the small  $\rho$  limit, the analytical expression

$$L_{k\rho}(x) = \left[ 1 - \frac{\rho^2}{2} \left( \operatorname{sech}^2 x + \frac{k^2}{2} \right) \right] \tanh x + \mathcal{O}(\rho^3), \quad (14)$$

along with its derivatives can be used to evaluate directly the right-hand-side of Eqs. (12) and (13) with no overhead computation time.

The Larmor radius of thermal ions in fusion plasmas is typically small, compared to the zonal flow width. However, this is not necessary the case for  $\alpha$ -particles produced by DT fusion reactions for which the Larmor radius may be actually larger than  $L$ , thus constituting a very important effect to take into consideration. For ITER parameters, a rough estimate of the size of the normalized gyroradius for alpha particles at birth gives  $\rho \sim 2$ , before losing their energy to the plasma. As the  $\alpha$ -particles thermalize, there will be a wider distribution of smaller Larmor radii but the mean of the normalized Larmor radius will typically stay greater than one.<sup>16</sup>

### III. ZONAL FLOW BIFURCATION AND PHASE SPACE TOPOLOGY

When FLR effects are neglected,  $\mathbf{u}_0 = u_0(x) \mathbf{e}_y \times \nabla \varphi_0$ , implies that a non-monotonic radial electric with a single extremum will always give rise to non-monotonic zonal flow with a single extremum. However, when  $\rho \neq 0$ , the zonal flow profile, is given by the gyro-average

$$v_0(x) = \frac{\partial \langle \varphi_0 \rangle_{\theta}}{\partial x} \equiv \langle u_0 \rangle_{\theta} = L'_{0\rho}(x), \quad (15)$$

which is not trivially related to the electric field profile. In particular, depending on the value of  $\rho$ , for a given electric field with a single extremum, the zonal flow can bifurcate from a profile with a single extremum to a profile with two maxima and one minimum. An example of this type of zonal flow bifurcation is shown in the right panel of Fig. 1 for  $\varphi_0 = \tanh x$  that corresponds to an  $\mathbf{E} \times \mathbf{B}$  guiding center velocity with a  $\operatorname{sech}^2 x$  profile. Extrema are important since they are related to shearless barriers that are very resilient to breakup due to chaos. The location of the zonal flow shearless barriers is defined as  $\sigma_0(x; \eta, \rho) = 0$  where

$$\sigma_0(x; \eta, \rho) = \frac{\partial^2 \langle \varphi_0 \rangle_{\theta}}{\partial x^2} = L''_{0\rho}(x). \quad (16)$$

As discussed in Ref. 8, for a  $\operatorname{sech}^2 x$  profile, when  $\rho \leq 1.33$  there is only one shearless region which corresponds to the single maximum of the zonal flow. However, for  $\rho > 1.33$ , the zonal flow bifurcates: the center becomes a minimum and two symmetrically located maxima are created as seen in the right panel of Fig. 1. The distance between the maxima grows linearly with  $\rho$ .

To derive general conditions for the bifurcation threshold, first note that, in Fourier space, the gyroaverage consists of the multiplication by the zeroth-order Bessel function,  $J_0(x)$ ,

$$\widehat{\langle u_0 \rangle_{\theta}}(k) = \hat{u}_0(k) J_0(k\rho), \quad (17)$$

where  $\hat{f} = \int_{-\infty}^{\infty} e^{ikx} f dx$ . From here, it follows that

$$\frac{d^n \langle u_0 \rangle_{\theta}}{dx^n} = \frac{(-i)^n}{2\pi} \int_{-\infty}^{\infty} k^n \hat{u}_0(k) J_0(k\rho) e^{-ikx} dk. \quad (18)$$



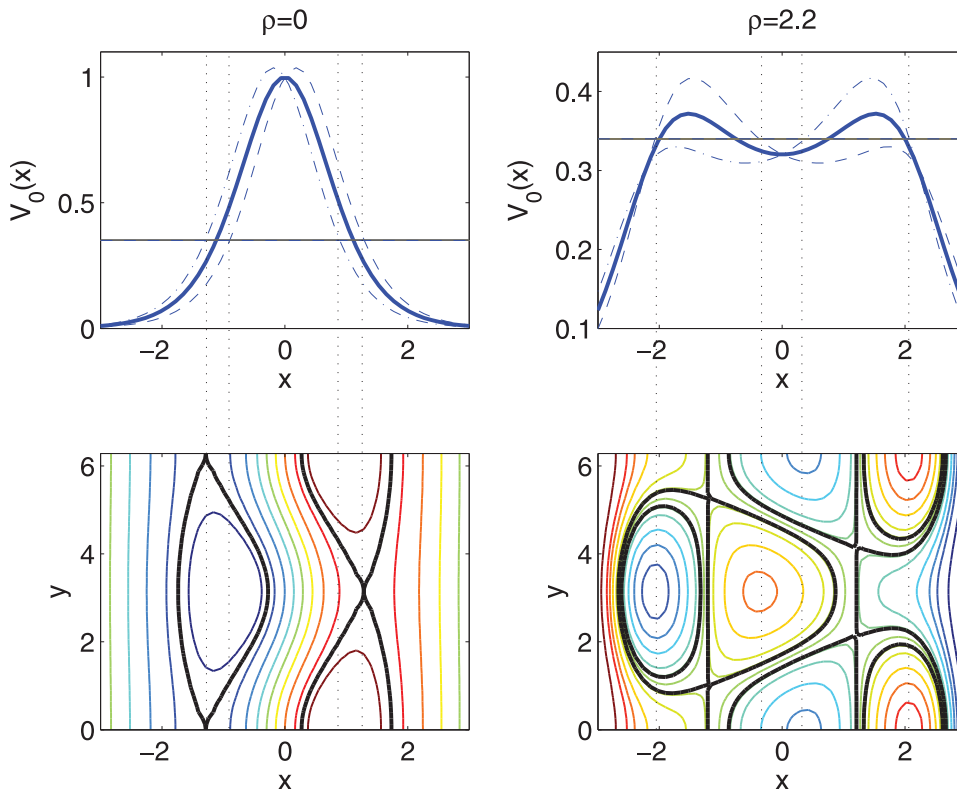


FIG. 1. Zonal flow bifurcation and corresponding phase space topology. Left panel: zero Larmor radius with  $\eta = 0.35, \epsilon_1 = 0.2, k_1 = 1$ . Right panel: gyroaverage over finite Larmor radius  $\rho = 2.2$  showing bifurcated zonal flow for  $\eta = 0.34, \epsilon_1 = 0.25, k_1 = 1$ . The dashed lines show the zonal flow with the drift wave perturbation at maximum and minimum amplitude.

As the previous studies for the special case of the  $\text{sech}^2 x$  zonal flow showed, the bifurcation of the zonal flow implies a change in the curvature of the velocity function at  $x = 0$ . In particular, it is assumed that for  $\rho = 0$ ,

$$\left. \frac{d^2 \langle u_0 \rangle_\theta}{dx^2} \right|_{x=0} = \left. \frac{d^2 u_0}{dx^2} \right|_{x=0} < 0. \quad (19)$$

After the bifurcation  $\left. \frac{d^2 \langle u_0 \rangle_\theta}{dx^2} \right|_{x=0} > 0$ , and thus, the threshold,  $\rho = \rho_*$ , is defined by the condition

$$\left. \frac{d^2 \langle u_0 \rangle_\theta}{dx^2} \right|_{x=0} = -\frac{1}{2\pi} \int_{-\infty}^{\infty} k^2 \hat{u}_0(k) J_0(k\rho_*) dk = 0. \quad (20)$$

As a tractable example consider a Gaussian zonal flow

$$u_0(x) = e^{-x^2/\sigma^2}, \quad \hat{u}_0(k) = \sqrt{\pi}\sigma e^{-\sigma^2 k^2/4}. \quad (21)$$

Using the identity<sup>17</sup>

$$\int_0^\infty x^2 e^{\alpha x^2} J_0(\beta x) dx = \frac{\sqrt{\pi}}{2\alpha\beta} e^{-\beta^2/(8\alpha)} M_{1,0}\left(\frac{\beta^2}{4\alpha}\right), \quad (22)$$

where  $M_{1,0}$  is the Whittaker function, we conclude that, for the Gaussian zonal flow, the critical Larmor radius is given by the zero of the Whittaker function,

$$M_{1,0}(\rho_*^2/\sigma^2) = 0. \quad (23)$$

The Whittaker function is related to the confluent hypergeometric function and can be computed numerically. According to Ref. 18, the number  $n$  of positive zeros of  $M_{\kappa,\mu}(z)$  is given by the smallest integer greater than or equal to

$d = \kappa - \mu - 1/2 > 0$ . Therefore,  $M_{1,0}$  has exactly one zero. That is, there exists a value of  $\rho$  for which the Gaussian zonal flow bifurcates.

As an alternative approach to find the bifurcation threshold, consider the Taylor expansion of the zonal flow

$$u_0(x) = \sum_{n=0}^{\infty} \frac{u_0^{(n)}(0)}{n!} x^n, \quad (24)$$

and write the second derivative of the gyroaveraged flow as

$$\frac{d^2 \langle u_0 \rangle_\theta}{dx^2} = \left\langle \frac{d^2 u_0}{dx^2} \right\rangle_\theta = \sum_{n=2}^{\infty} \frac{n(n-1)}{n!} u_0^{(n)}(0) \langle x^{n-2} \rangle_\theta. \quad (25)$$

From here, it follows that

$$\left. \frac{d^2 \langle u_0 \rangle_\theta}{dx^2} \right|_{x=0} = \frac{1}{2\pi} \sum_{m=0}^{\infty} \frac{u_0^{(m+2)}(0)}{m!} \rho^m \int_0^{2\pi} (\cos \theta)^m d\theta, \quad (26)$$

which implies the following necessary and sufficient condition for the zonal flow bifurcation condition and the corresponding threshold value  $\rho_*$ ,

$$\begin{aligned} \left. \frac{d^2 \langle u_0 \rangle_\theta}{dx^2} \right|_{x=0} &= u''(0) + \sum_{m=1}^{\infty} \frac{(2m-1)!!}{(2m)!(2m)!!} u_0^{(2[m+1])}(0) \rho_*^{2m} \\ &= 0. \end{aligned} \quad (27)$$

For the Gaussian zonal flow, using the relation,

$$\frac{d^n}{dx^n} e^{-(x/\sigma)^2} = \frac{(-1)^n}{\sigma^n} e^{-(x/\sigma)^2} H_n(x/\sigma), \quad (28)$$

where  $H_n$  are the Hermite polynomials of order  $n$ , we conclude that the threshold  $\rho_*$  is given by the solution of

$$\begin{aligned} \sigma^2 \frac{d^2 \langle u_0 \rangle_\theta}{dx^2} \Big|_{x=0} &= -2 + \sum_{m=1}^{\infty} \frac{(2m-1)!!}{(2m)!(2m)!!} H_{2(m+1)}(0) \left(\frac{\rho_*}{\sigma}\right)^{2m} \\ &= 0. \end{aligned} \tag{29}$$

The first step to understand the effect of the normal modes on transport is to study the resonances located at the place(s) where the propagation velocity of the modes matches the velocity of the zonal flow. According to Eq. (9), the gyroaveraged Hamiltonian with a single mode in the co-moving reference frame is given by

$$\langle \phi_0 \rangle_\theta = L_{0\rho}(x) - \eta x + \varepsilon_1 L'_{k_1\rho}(x) \cos(k_1 y), \tag{30}$$

and the location of the resonances is determined by the condition

$$R(x; \rho, \eta) = \frac{\partial \langle \phi_0 \rangle_\theta}{\partial x} - \eta = L'_{0\rho}(x) - \eta = 0. \tag{31}$$

Figure 2 shows the dependence on  $\rho$  of the location of the resonances according to Eq. (30) for several values of  $\eta$ . Consistent with the fact that for small values of  $\rho$  the zonal flow has a single maximum, in this case there can be zero or at most two resonances. However, for large values of  $\rho$ , when  $\eta$  is in a range corresponding to wave velocities between the maxima and the minimum of the gyroaveraged flow profile, there can be up to four resonances. The resonances are important because they are the seeds for the growth of islands created by the perturbation. Thus, in this case, as  $\rho$  increases, there can be two or four chains of islands. The bold line in Fig. 2 corresponding to  $\eta = 0.34$  shows an example of four resonances for a value of  $\rho = 2.2$  marked by the horizontal dashed line. This is the same case represented in the right panel of Fig. 1 which also shows four resonances and the corresponding double chain of islands in phase space.

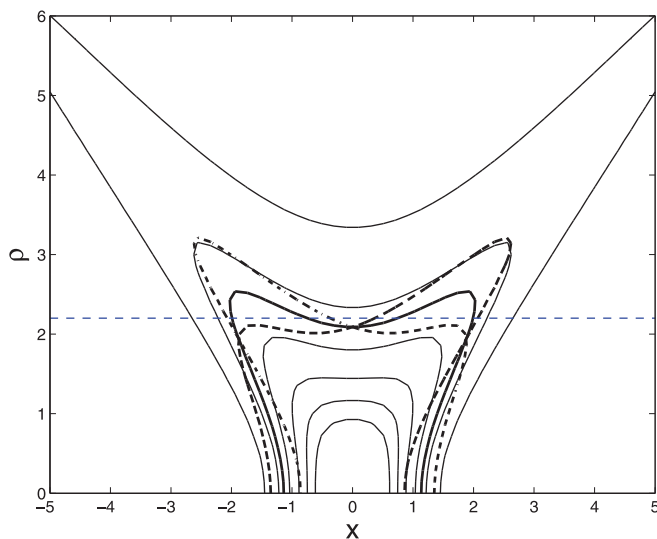


FIG. 2. Location of the resonance layers given by  $R(x; \eta, \rho) = 0$  when  $\rho$  is varied, for  $\eta = 0.2, 0.3, 0.4, 0.5$  and  $0.6$  from top to bottom, respectively. The value  $\eta = 0.34$ , shown with the bold line, is the same used in the right panel of Fig. 1, for which the fixed points of the single-mode Hamiltonian are also shown (for  $\varepsilon_1 = 0.25$ ) with the bold dashed line for even and dot-dashed line for odd  $n$  in Eq. (32). The crossings with  $\rho = 2.2$  correspond to the (elliptic) O-points.

The fixed points  $(x_*, y_*)$  for the single mode gyroaveraged Hamiltonian in Eq. (30) are defined by the condition  $\partial_x \langle \phi \rangle_\theta(x_*, y_*) = \partial_y \langle \phi \rangle_\theta(x_*, y_*) = 0$ , which has a family of solutions given by,

$$y_* = \pi n / k_1, \quad \eta - L'_{0\rho}(x_*) - (-1)^n \varepsilon_1 L''_{k_1\rho}(x_*) = 0. \tag{32}$$

The bold dashed lines in Fig. 2 follow the location of fixed points with  $n$  even and odd, for  $\eta = 0.34$  and  $\varepsilon_1 = 0.25$ . As shown on the right-bottom panel of Fig. 1, in this case, there are four fixed points (two stable and two unstable). For comparison, Fig. 1 also shows with dashed lines, the zonal flow  $v_x = \partial_x \langle \phi_0 \rangle_\theta + \eta$ , according to Eq. (30) for  $y=0$  and  $y = \pi/k_1$  which also correspond to the solutions of Eq. (32) for the resonant modes  $v_x = \eta$ ; thus these also indicate the location of hyperbolic and elliptic points as marked by the vertical lines.

When there is only one mode, the system is integrable and the topology of the trajectories is determined by the isocontours of the Hamiltonian. However, like in the case of non-twist Hamiltonian systems,<sup>19,20</sup> the topology can change because of separatrix reconnection. In particular, as Fig. 3 shows, for a finite value of the Larmor radius, an increase of the mode amplitude  $\varepsilon_1$  can lead to a change in the topology from heteroclinic (in which the two branches of the separatrix link different hyperbolic fixed points of the same resonance) to homoclinic (in which one of the branches of the separatrix links the same hyperbolic fixed point). As shown in the middle panel of Fig. 3, the separatrix reconnection leading to the change of the topology has a threshold in which the two branches of the separatrix link different hyperbolic fixed points of different resonances. However, what is interesting is that, as shown in Fig. 4, FLR effects by themselves can cause separatrix reconnection. In particular, an increase of the Larmor radius from  $\rho = 0.5$  to  $\rho = 1.7$  changes the topology from heteroclinic to homoclinic. Remarkably, as the right panel of Fig. 4 shows, a further increase of the Larmor radius to  $\rho = 3$  causes the trapping regions to disappear, and “rectifies” the flow into an almost parallel dynamics.

The complexity of the possible separatrix reconnection scenarios increases for parameter values for which the zonal flow exhibits two maxima and a minimum as shown, for example, in the right panels of Fig. 1. In this case, there can be up to four chains of fixed points (see Fig. 2) and the different hyperbolic points can be linked in multiple ways as shown in Fig. 5. Another case is the doublet topology presented in the last panel of Fig. 1. As the gyroradius is increased there are reconnections at various points between separatrices leading to topologies from nested separatrix, to the formation of cusps when a fixed point disappears, to two island chains in phase that contain three zonal flows. In the following, we consider Larmor radii smaller than the bifurcation threshold, as these are the cases more likely to be encountered in fusion experiments.

#### IV. FLR EFFECTS ON CHAOTIC TRANSPORT

When two modes are present, i.e., for  $\varepsilon_1 \neq 0$  and  $\varepsilon_2 \neq 0$ , the equations of motion in Eqs. (12) and (13) are not

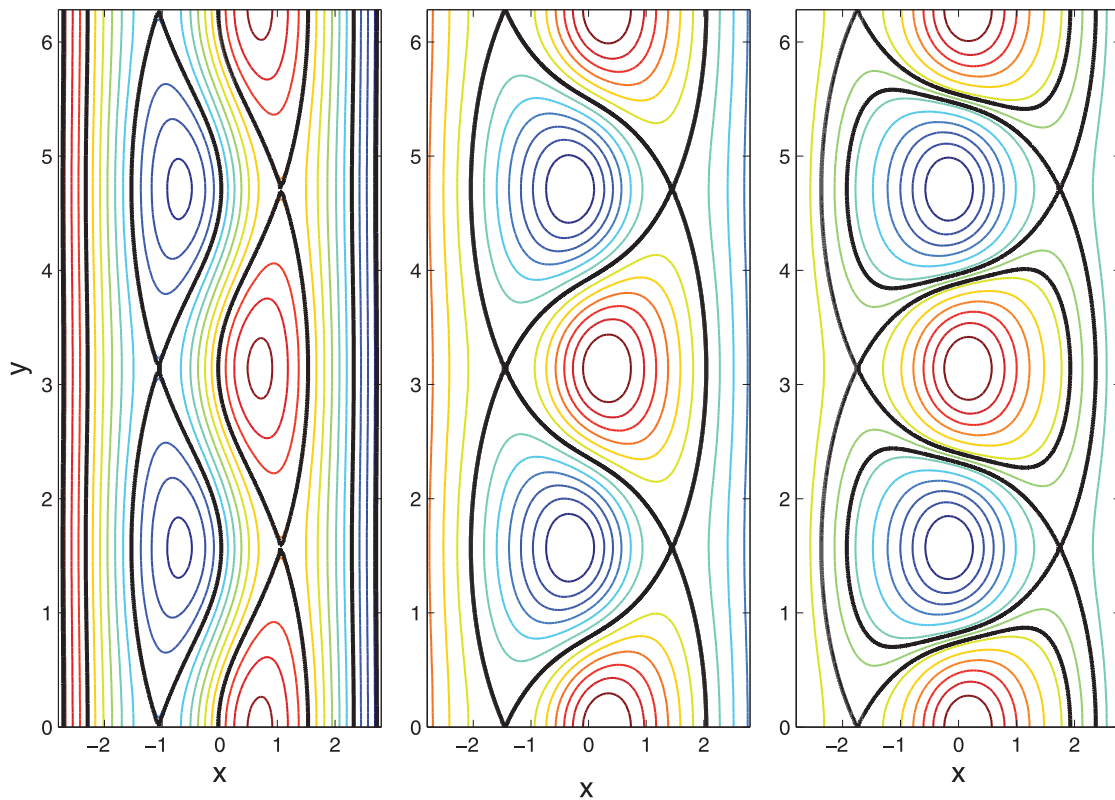


FIG. 3. Topology change through separatrix reconnection when  $\varepsilon_1$  is increased from 0.2 to 0.855 to 1.8 for  $\rho = 0.2$  and  $\eta = 0.5$ . First panel has heteroclinic topology, second panel is the reconnection threshold and third panel has homoclinic topology.

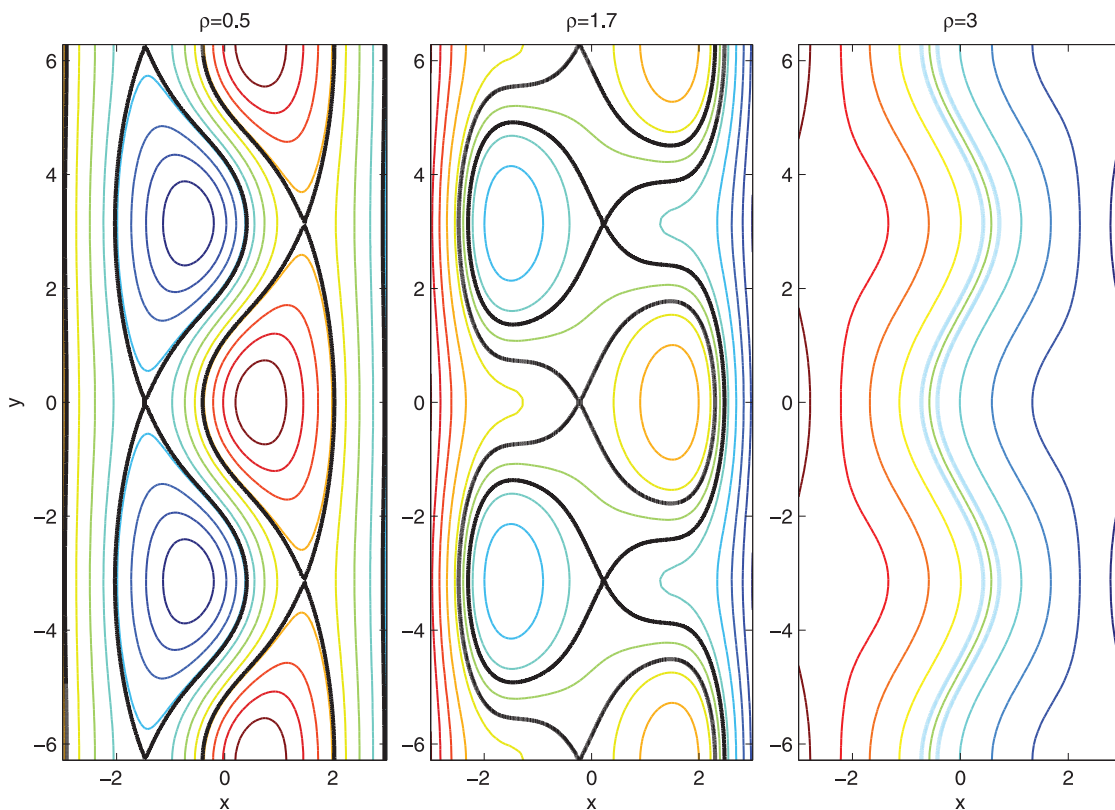


FIG. 4. Finite Larmor radius effects on phase space topology for the gyroaverage Hamiltonian in Eq. (30) with  $\varepsilon_1 = 0.5$ ,  $k_1$  and  $\eta = 0.4$ . As  $\rho$  increases from  $\rho = 0.5$  to  $\rho = 3$ , separatrix reconnection changes the topology from heteroclinic to homoclinic and ends with flow rectification.

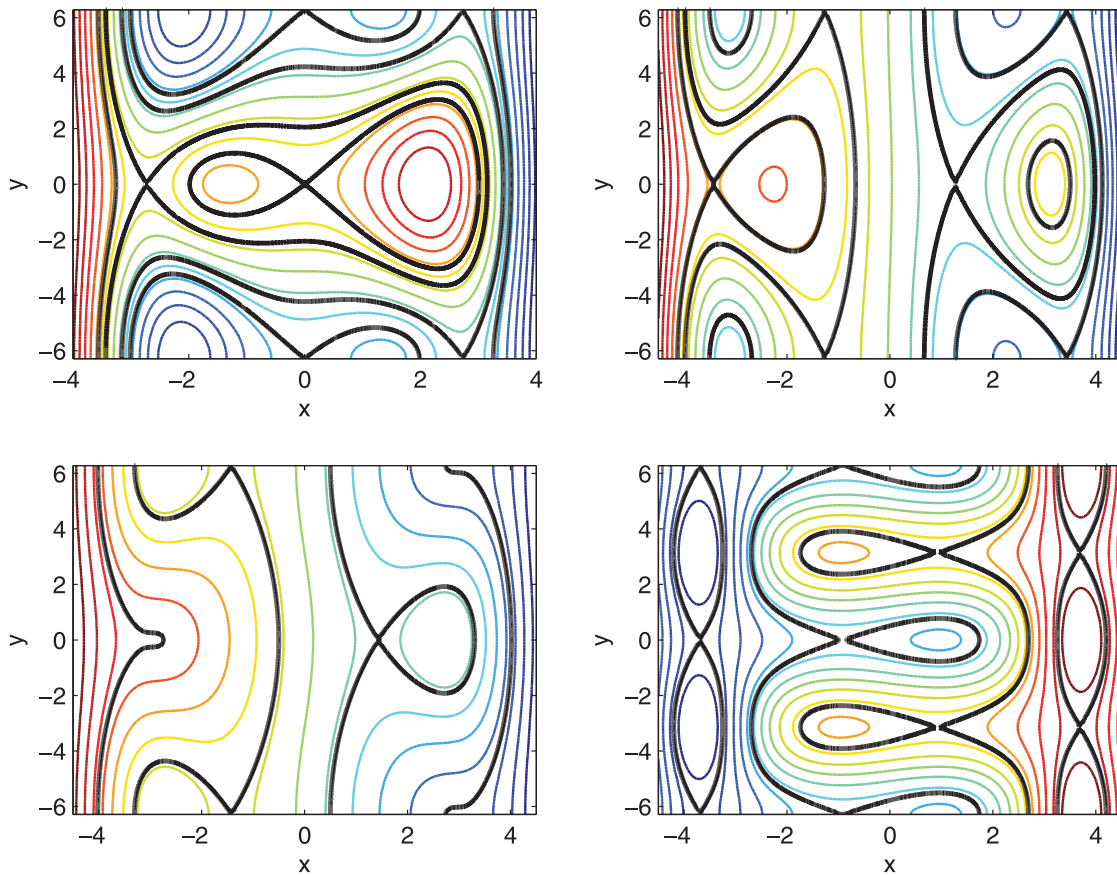


FIG. 5. Gyroradius-average-induced separatrix reconnection for increasing  $\rho$ : Top-left panel is for  $\rho = 2.3312, \eta = 0.3, \varepsilon_1 = 0.5$  and  $k_1 = 0.5$ . Top-right panel is for  $\rho = 3.0748, \eta = 0.3, \varepsilon_1 = 0.5$  and  $k_1 = 0.5$ . Bottom-left panel corresponds to  $\rho = 3.25, \eta = 0.25, \varepsilon_1 = 0.3$  and  $k_1 = 0.5$ . Bottom-right has  $\rho = 3.5, \eta = 0.2, \varepsilon_1 = 0.25$  and  $k_1 = 1$ .

integrable in general and test particles can exhibit chaotic transport. The goal of this section is to study the role of gyro-averaging on this phenomenon. In particular, we show that FLR effects tend to reduce, and even suppress, chaotic transport.

### A. Chaotic transport suppression

As it is well-known, for time-periodic perturbations, the dynamics can be represented in a Poincaré plot on which integrable orbits trace well-defined smooth 1-dimensional curves, while chaotic orbits spread in a seemingly random way over the 2-dimensional domain. The Poincaré plots in Fig. 6 show numerical evidence of chaos suppression due to FLR effects in the heteroclinic topology. For a small Larmor radius, and large enough wave amplitude ( $\varepsilon_2 = 0.05$  in this case), the shearless central transport barrier has been destroyed and there is global chaos allowing particles to cross freely from left to right in  $x$ . However, as the Larmor radius increases, the chaotic region is reduced and for large enough values of  $\rho$  (in this case,  $\rho = 0.75$ ), the particle trajectories follow closed orbits and transport along the  $x$  direction is suppressed. A similar situation is observed in Figure 7 for the homoclinic topology. As before, for small  $\rho$ , large chaotic regions are observed, although in this case a meandering shearless central transport barrier is present. As the Larmor radius increases, the chaotic regions are reduced, and for  $\rho = 0.75$ , all the trajectories are regular. It is interesting

to note that the observed suppression of transport occurs for  $\rho$  values within the range of the typical Larmor radii for alpha particles in burning plasmas.

### B. Transport barriers restoration

The shearless curve is directly associated with the transport barrier produced by the presence of the zonal flow, and for this reason, it is important to determine the properties of this curve. The location of the shearless barrier (when it exists) can be determined using the indicator point method proposed in Ref. 21 and used in Ref. 22 to detect the shearless transport barriers in a meandering flow. The method is based on the existence of certain symmetries in the equations of motion for the test particles. It is readily seen that Eqs. (12) and (13) for  $k_1 = k_2$  are invariant under the transformation

$$S = \begin{cases} x' = -x \\ y' = y + \pi/k_1. \end{cases} \quad (33)$$

On the other hand, the equations have also the time reversal symmetry

$$I_0 = \begin{cases} x' = x \\ y' = -y. \end{cases} \quad (34)$$

Let  $G_t$  be the evolution operator defined by the solution of Eqs. (12) and (13) at time  $t$ . Then, the evolution operator  $G_T$ ,



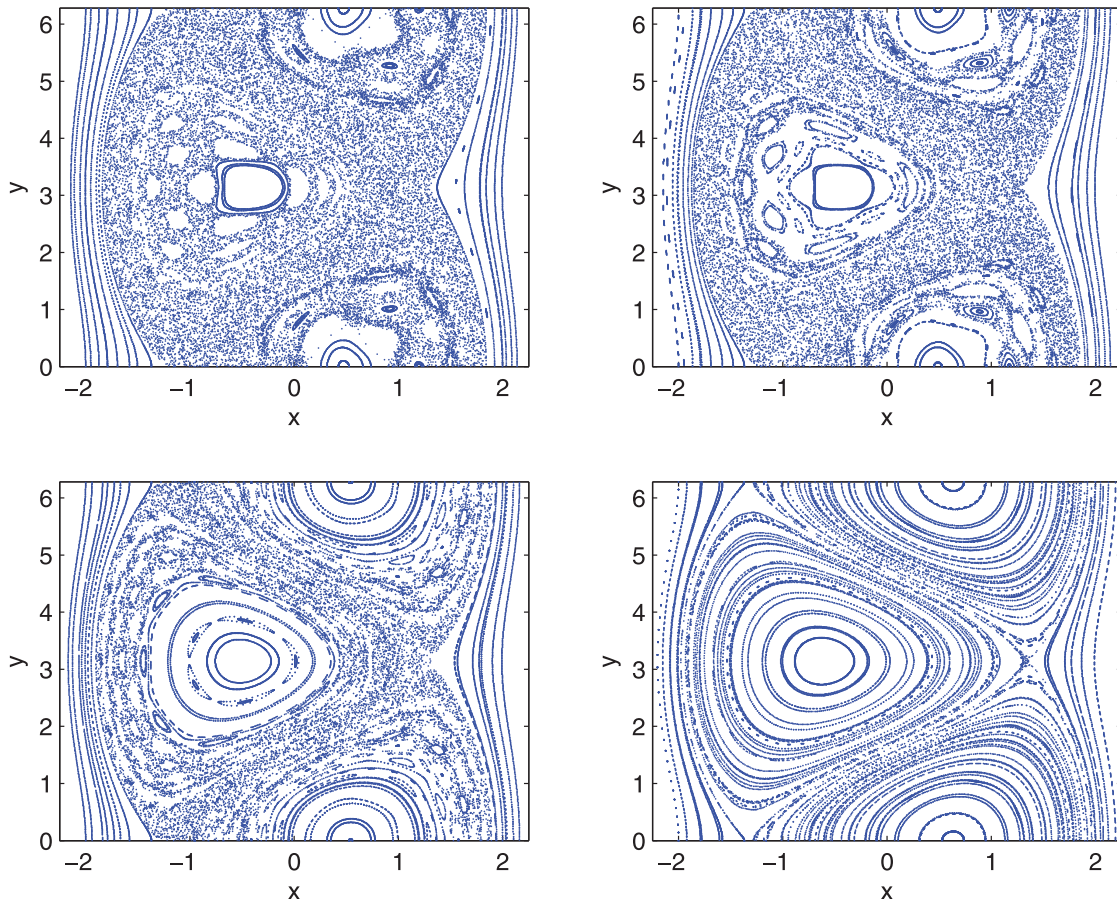


FIG. 6. Gyroaverage induced chaotic transport suppression in the heteroclinic topology for parameters  $\omega = 2.3, \eta = 0.5, \epsilon_1 = 0.5, \epsilon_2 = 0.05, k_1 = 1, k_2 = 2$ .

where  $T$  is the period of the perturbation, can be expressed as the composition of two involutions  $I_0, I_1$ , as  $G_T = I_1 I_0$ , where  $I_0$  is given by Eq. (34) and  $I_1 = G_T I_0$ , which have the property  $I_0 I_0 = I_1 I_1 = 1$ . The indicator points (IP) are defined as those satisfying  $I_0(x, y) = S(x, y)$  or  $I_1(x, y) = S(x, y)$ , the later being equivalent to finding the solutions of

$$G_T(x, y) = S I_0(x, y) = (-x, -y + \pi/k_1). \quad (35)$$

Following Ref. 22, we solve this equation by finding the minimum of the function

$$r(x, y) = \|G_T(x, y) - (-x, -y + \pi/k_1)\| \quad (36)$$

that satisfies  $r(x, y) = 0$ . Other IPs can also be defined by  $I_0(x, y) = S(x, y)$ .

Since IPs belong the shearless curve (SC), they can be iterated with the operator  $G_T$  to generate a Poincaré section of the SC. Since it can also be shown<sup>21</sup> that the involutions  $I_0$  and  $I_1$  map the SC onto itself, they can be used to obtain new IPs from known ones. Using the symmetries, one can get the following IPs, associated with the involution  $I_0$ :  $(0, (1 + 1/2k_1)\pi)$ ,  $(0, \pi/2k_1)$  and  $(0, (1 - 1/2k_1)\pi)$ ,  $((2 - 1/2k_1)\pi)$  provided  $k_1 > 1/2$ . The IP associated with the involution  $I_1$  which is a solution to Eq. (35) is a point in the neighborhood of  $(0, 1)$ ; it changes as the parameters of the map (such as  $\epsilon_2$  and  $\rho$ ) are modified.

Figure 8 shows the SC embedded in the map of the particle trajectories obtained from the integration of Eqs. (12) and (13) in the heteroclinic case (left panel). In this case, the SC acts as an effective barrier to transport, i.e., despite the fact that most of particle trajectories are chaotic, the region around the SC is not crossed by the particles. A similar situation is observed in the homoclinic topology case shown also in the right panel of Figure 8.

Using the indicator points, we mapped the SC for different parameters of the system. For small  $\rho$  and  $\epsilon_2$  the SC is a well defined 1-D curve and acts as a central transport barrier (CTB). As the value of  $\epsilon_2$  is increased the SC becomes stochastic and it no longer forms a curve. However, a CTB can still prevent the crossing of particles. Finally, for large enough  $\epsilon_2$  the SC chaotically fills a global 2D domain indicating that the transport barriers are all destroyed and the map exhibits global transport. The transition through these stages is shown in Figure 9. The criterion to determine when the CTB is destroyed adopted in Refs. 21 and 22, is that it occurs when the map of the IP reaches global chaos, and that is established when the map is unbounded in the  $y$ -direction. Here, we observe a particular behavior for the evolution of the IP map as  $\epsilon_2$  grows. First, the map is always contained within the unperturbed (for  $\epsilon_2 = 0$ ) outer separatrix boundaries; thus, in spite of the appearance of a global chaos, it never goes beyond those boundaries. Second, before global chaos appears there is the so-called banded chaos regime, where the chaotic motion of the IP is contained between the

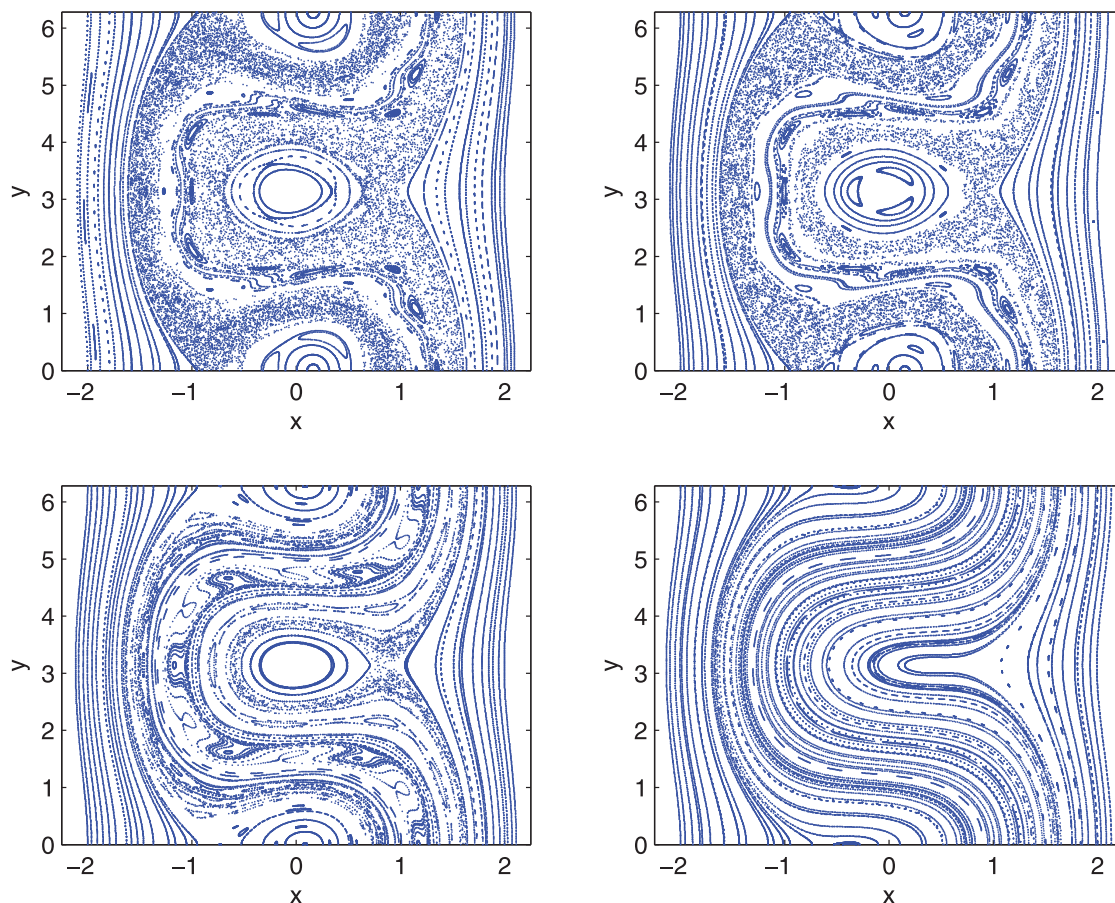


FIG. 7. Gyroaverage induced chaotic transport suppression in the homoclinic topology for parameters  $\omega = 2.3, \eta = 0.85, \epsilon_1 = 0.6, \epsilon_2 = 0.05, k_1 = 1, k_2 = 2$ .

CTB and one of the outer separatrices (either one of them can occur). This can be seen in Fig. 9. The establishment of banded chaos occurs when  $\epsilon_2$  exceeds a threshold value for a given  $\rho$ . When Larmor radius is increased, the barrier can be restored as shown in the Poincaré map of Figure 6 for  $\rho = 0.75$ . An example of the homoclinic mapping is given in Figure 7 which shows a clear transport barrier. The question then arises of how FLR affects the destruction of the SC.

The threshold for the destruction of the CTB in the  $\rho - \epsilon_2$  plane is shown in Fig. 10. The threshold was computed by fixing  $\rho$  and increasing  $\epsilon_2$  until the mapping of the IP reaches either separatrix after 50 000 iterations. This was made for both heteroclinic and homoclinic topologies. When  $\epsilon_2$  is further increased a second threshold value is obtained when global chaos is established. At this point, the IP map reaches the separatrices on both sides but quite often this

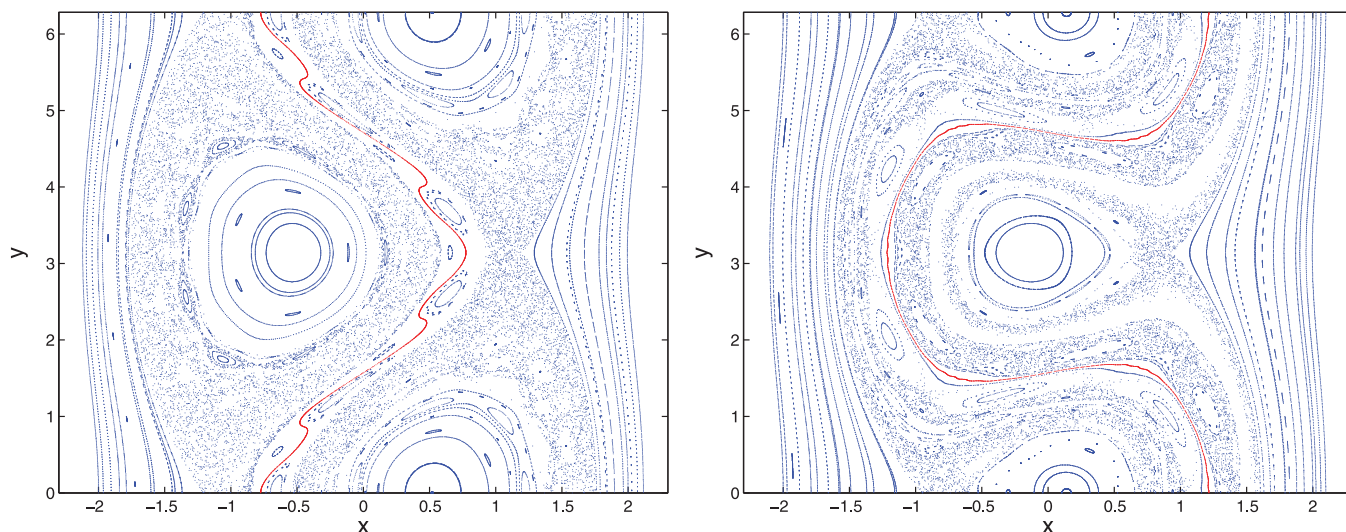


FIG. 8. Shearless curve (red) embedded in the Poincaré map of 80 particles for  $\rho = 0.1, \omega = 2.3, \epsilon_2 = 0.05$  in the (a) heteroclinic ( $\eta = 0.5, \epsilon_1 = 0.4$ ) and (b) homoclinic ( $\eta = 0.85, \epsilon_1 = 0.5$ ) topologies. In both cases, the shearless curve is a robust transport barrier.



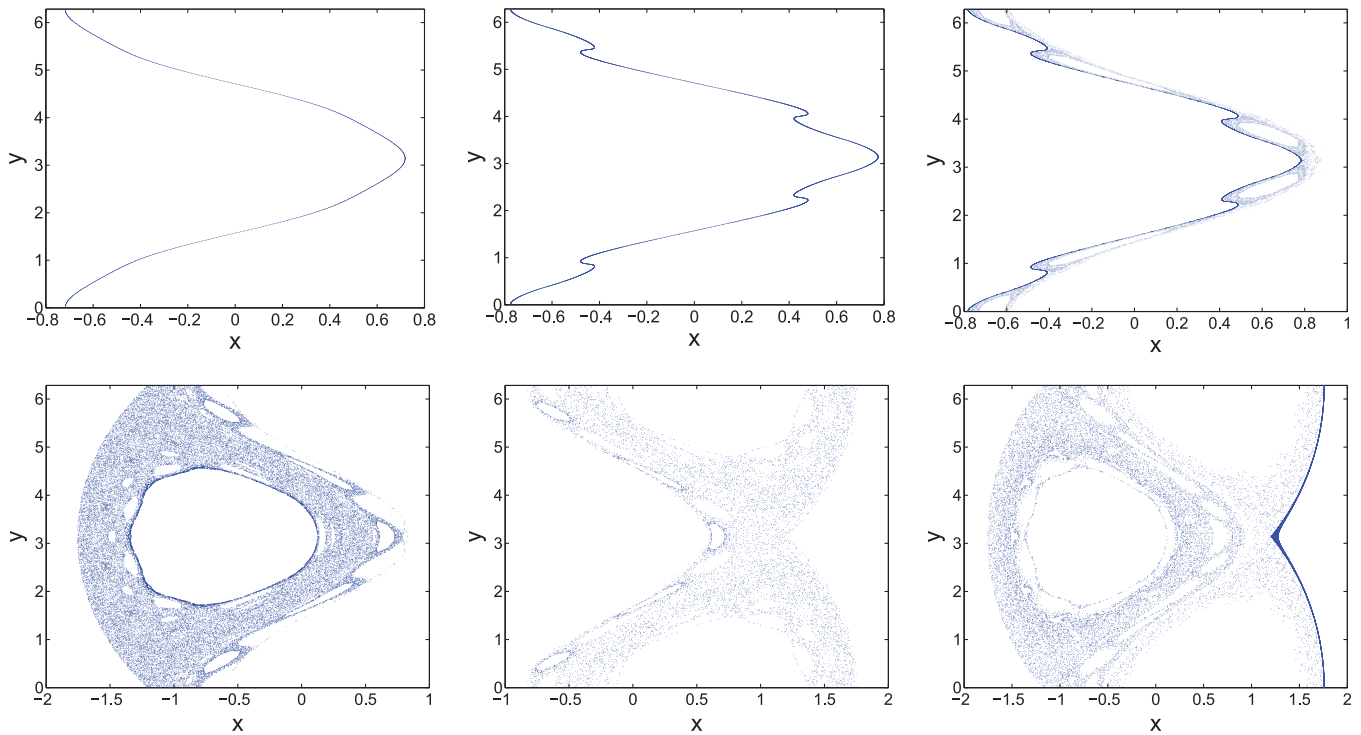


FIG. 9. Evolution of the shearless curve as the parameter  $\varepsilon_2$  is increased, showing the destruction of the curve and the transition to a stochastic layer and to global chaos. Here  $\omega = 2.3$ ,  $\eta = 0.5$ ,  $\varepsilon_1 = 0.4$ ,  $\rho = 0.1$ ; from top left to bottom right  $\varepsilon_2 = 0.01, 0.05, 0.054, 0.06, 0.07, 0.075$ .

takes a much larger number of iterations; for some parameters, the map seems to be contained to one side of an apparent barrier after 50 000 iterations but when it is followed for longer times it starts filling the other side (last panel in Figure 9). For these cases, it is necessary to use 80 000 iterations. There is still some doubt that the cases that appear to be contained on one side of the barrier (possibly corresponding to banded chaos), might eventually fill the whole region for a large enough number of iterations. This has not been possible to confirm because of the very long time it takes to integrate the map for iterations of the order of  $10^5$ . With this caveat, the second threshold, for global chaos, was obtained and

represented in a  $\rho - \varepsilon_2$  diagram. The results presented are reliable to within a number of iterations equal to or smaller than  $10^5$ .

As seen in the  $\rho - \varepsilon_2$  threshold diagrams, the dependence is not monotonic since as  $\rho$  increases the threshold value of  $\varepsilon_2$  varies up and down creating a fractal-like boundary. The threshold values were computed by starting from  $\varepsilon_2 = 0$  for a given  $\rho$ , and then increasing  $\varepsilon_2$  in steps of  $\Delta\varepsilon_2 = 0.002$  computing at each step the SC, until one of the above criteria for chaotic SC is met. Then, the position of the threshold is refined up to a precision of  $\delta\varepsilon_2 = 0.0003$ . Then, the value of  $\rho$  is increased in steps of  $\Delta\rho = 0.004$  following

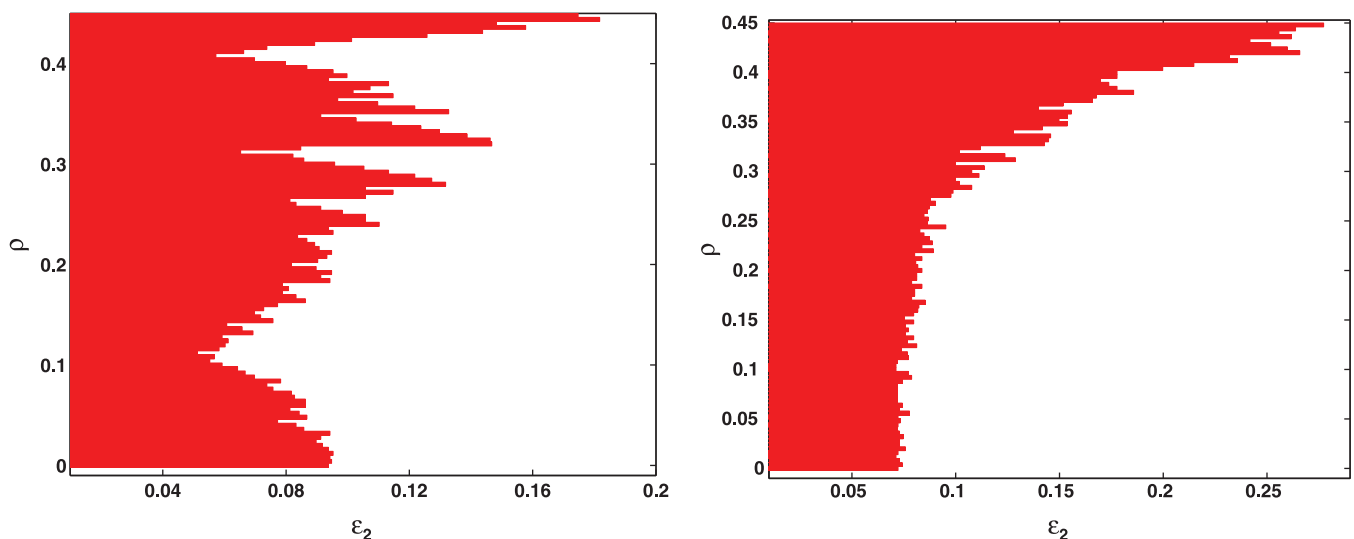


FIG. 10. Threshold for the destruction of the shearless curve for  $\omega = 2.3$ ,  $k_1 = k_2 = 1$  for (a) heteroclinic geometry when  $\rho = 0$  ( $\eta = 0.5$ ,  $\varepsilon = 0.4$ ) and (b) homoclinic geometry for  $\rho = 0$  ( $\eta = 0.85$ ,  $\varepsilon = 0.5$ ).

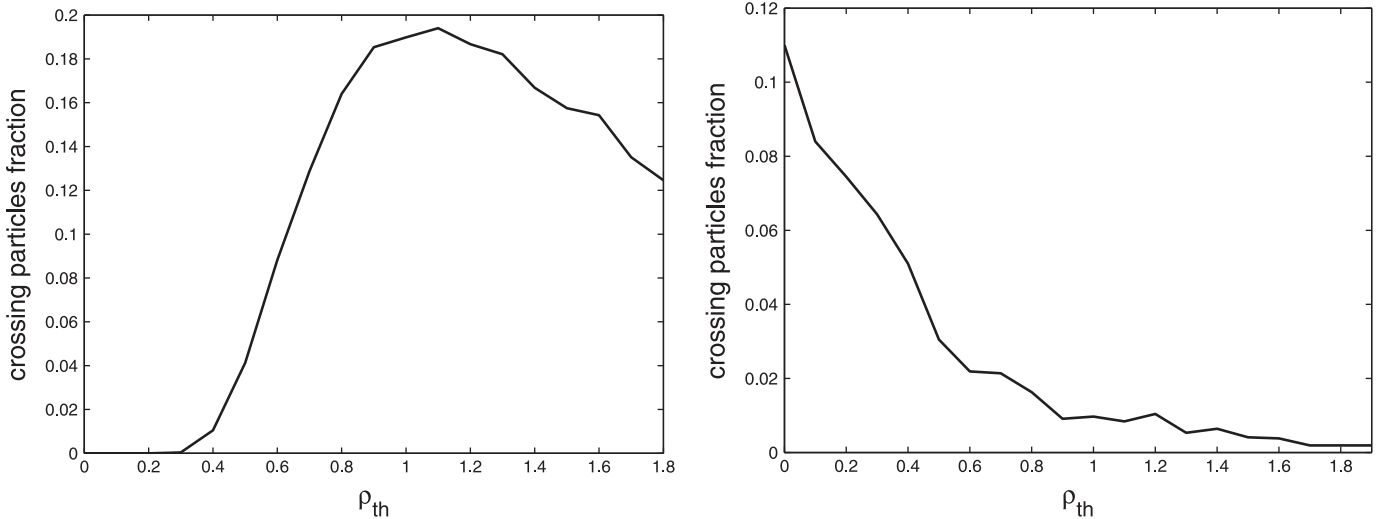


FIG. 11. Fraction of thermal particles crossing from one side to the other of the barrier that would be present when  $\rho = 0$ , corresponding to (a) heteroclinic topology when  $\rho = 0$  ( $\eta = 0.5, \varepsilon_1 = 0.4, \varepsilon_2 = 0.07$ ) and (b) homoclinic topology when  $\rho = 0$  ( $\eta = 0.85, \varepsilon_1 = 0.6, \varepsilon_2 = 0.12$ ). In both cases  $\omega = 2.3$  and  $k_1 = k_2 = 1$ .

the same procedure for each value of  $\rho$ . Therefore, the plots are accurate up to the precision  $\Delta\rho$  and  $\delta\varepsilon_2$ ; thus if there is a chaotic IP map in a window smaller than  $\delta\varepsilon_2$  it cannot be detected by our procedure. This is important due to the fractal structure of the threshold boundary, which is similar to the fractal boundary found in Refs. 21 and 22 in the  $\omega - \varepsilon$  space (perturbation frequency and amplitude).

## V. THERMALLY DISTRIBUTED LARMOR RADII

In a thermal plasma, the kinetic energy of the particles and their corresponding Larmor radii have a Maxwellian distribution. According to the previous results, particles with different  $\rho$  experience different gyro-averaged electric fields and thus different levels of chaos suppression. Thus, in order to assess the extent to which a transport barrier is present in a plasma with a finite temperature, we need to consider ensembles of test particles with different Larmor radii. We do this by considering a thermal distribution of  $\rho$  for an ensemble of particles located on a localized region on one side of a  $\rho = 0$ -barrier (that is, a transport barrier for particles with  $\rho = 0$ ). We then follow each particle in the ensemble for a large number of iterations in a Poincaré plot and determine if each particle has reached the other side of the barrier. After this process is done for all the particles, the fraction of particles crossing to the other side of the  $\rho = 0$ -barrier,  $f$ , is computed. This gives an estimate of the effectiveness of the transport barrier: for  $f = 1$  the barrier is destroyed while for  $f = 0$  there is a fully developed barrier.

In order to define  $f$  in an operational way, we introduce the binary function  $\Delta(\rho, \vec{r})$  which is equal to one when a particle with a given  $\rho$  and located initially at position  $\vec{r}$  crosses to the other side, and zero when it does not cross. The initial location and the crossing criterion are different for each topology and we will address this afterwards. In terms of  $\Delta$ , the fraction of particles crossing is given by,

$$f = \int \Delta(\rho, \vec{r}) f_m(\rho) d\rho d\vec{r}, \quad (37)$$

where the Maxwellian distribution is  $f_m(\rho) = (2\rho/\rho_{th}^2) \exp[-(\rho/\rho_{th}^2)]$  and  $\rho_{th}$  is the thermal Larmor radius. For the case with an heteroclinic topology at  $\rho = 0$ , the group of particles is located around the left separatrix X-point, within a region of the size of the distance from the X-point to the nearby shearless curve. In this way, we assure that all particles are on one side of the  $\rho = 0$ -barrier and none should be able to cross the flow. On the other hand, for the case of homoclinic topology for  $\rho = 0$ , all particles are located on one side of the left separatrix, between the X-point and the left-lying shearless curve. In this way, we also assure that all particles are to the left of the possible barrier.

In Fig. 11, we show the results of the fraction of particles crossing to the right in the two topologies. In the heteroclinic case, there is a maximum value of  $f$  for a certain  $\rho_{th}$ . For lower temperatures, the barrier is effective in blocking particles since the drift-wave amplitude is not high enough for most particles. For larger temperatures, the FLR barrier restoration is the responsible mechanism for not having particles crossing the flow. In the homoclinic case, corresponding to higher level of fluctuation from the onset, there is no barrier at  $\rho = 0$ , this is reflected in the fact that  $f \neq 0$  at  $\rho_{th} = 0$ . In this case, transport barrier restoration leads to a decrease in  $f$  as temperature increases.

## VI. SUMMARY AND CONCLUSIONS

We have shown that the inclusion of FLR effects through the gyroaveraging of the  $\mathbf{E} \times \mathbf{B}$  Hamiltonian plays a critical role in chaotic transport in non-monotonic zonal flows in the presence of drift-waves. The gyroaverage smooths out the trapping regions, since a particle typically samples regions with trapped and circulating topologies. When the Larmor radius is large enough, a single meandering zonal flow is what a particle “sees” and thus, cross-flow transport is completely suppressed. Another interesting feature is the bifurcation of the zonal flow. The flow has a single maximum for small Larmor radius,  $\rho$ , but its width increases with  $\rho$  and at a critical value



it bifurcates to two maxima and a minimum. This bifurcation can lead to the appearance of four resonances, instead of two, for a given mode. Because of this, the changes in the topology due to separatrix reconnection can be very rich and complex. We have also shown that FLR effects tend to reduce chaotic transport. In particular, the restoration of destroyed transport barriers is numerically observed as the Larmor radius increases. FLR effects lessen the action of the modes and tend to maintain the transport barriers. This is due to the smoothing out effect of the trapping regions mentioned before. FLR effects tend to restore the barrier by suppressing chaotic transport. The boundary for the destruction of the central transport barrier in the  $\rho - \varepsilon_2$  plane exhibits a fractal-like structure. However, it shows a general tendency that the barrier destruction threshold for the fluctuation amplitude increases with the Larmor radius. This fractal-like boundary is reminiscent of the one found in Ref. 22 in the fluctuation amplitude-frequency plane. Because of this, each particle with a given  $\rho$  experiences a different threshold for barrier destruction and therefore, for a thermal plasma, it is necessary to consider the collection of all particles in order to determine how effective a transport barrier can be. This was done in order to obtain the fraction of particles confined by the CTB, which provides the barrier efficiency for different temperatures at certain fluctuation levels. These results are potentially relevant for future burning plasma experiments where alpha particles will typically have large Larmor radii. According to the results presented, FLR effects will provide a better confinement for these particles when zonal flows are present. In particular, the effectiveness of barriers to chaotic transport of  $\alpha$ -particles is expected to improve as the temperature increases.

Finally, it is important to point out that the test particle approach we have followed in the present study is not self-consistent. In particular, the effects of the particle dynamics on the plasma have not been taken into account. Self-consistency may be important when studying strong turbulence and resonant wave-particle interactions. The study of this interesting phenomena is beyond the scope of the work presented here.

## ACKNOWLEDGMENTS

This work was sponsored by the Oak Ridge National Laboratory, managed by UT-Battelle, LLC, for the U.S. Department of Energy under Contract No. DE-AC05-00OR22725, and by projects PAPIIT-UNAM IN106911 and Conacyt 152905, Mexico.

- <sup>1</sup>P. W. Terry, *Rev. Mod. Phys.* **72**, 109 (2000).
- <sup>2</sup>J. Sommeria, S. D. Meyers, and H. L. Swinney, "Experiments on Vortices and Rossby Waves in Eastward and Westward Jets," in *Nonlinear Topics in Ocean Physics*, edited by A. Osborne (North-Holland, Amsterdam, 1991).
- <sup>3</sup>D. del-Castillo-Negrete and P. J. Morrison, *Phys. Fluids A* **5**, 948 (1993).
- <sup>4</sup>D. del-Castillo-Negrete, *Phys. Plasmas* **7**, 1702 (2000).
- <sup>5</sup>F. A. Marcus, I. L. Caldas, Z. O. Guimaraes Filho, P. J. Morrison, W. Horton, Y. K. Kuznetsov, and I. L. Nascimento, *Phys. Plasmas* **15**, 112304 (2008).
- <sup>6</sup>D. Toufen, Z. Guimaraes Filho, I. L. Caldas, F. A. Marcus, and K. W. Gentle, *Phys. Plasmas* **19**, 012307 (2012).
- <sup>7</sup>K. Gustafson, D. del-Castillo-Negrete, and W. Dorland, *Phys. Plasmas* **15**, 102309 (2008).
- <sup>8</sup>D. del-Castillo-Negrete and J. J. Martinell, *Commun. Nonlinear Sci. Numer. Simul.* **17**, 2031 (2012).
- <sup>9</sup>W. W. Lee, *J. Comput. Phys.* **72**, 243 (1987).
- <sup>10</sup>G. Manfredi and R. Dendy, *Phys. Rev. Lett.* **76**, 4360 (1996).
- <sup>11</sup>S. V. Annibaldi, G. Manfredi, and R. O. Dendy, *Phys. Plasmas* **9**, 791 (2002).
- <sup>12</sup>J. M. Dewhurst, B. Hnat, and R. O. Dendy, *Plasma Phys. Controlled Fusion* **52**, 025004 (2010).
- <sup>13</sup>A. Hasegawa and K. Mima, *Phys. Fluids* **21**, 87 (1978).
- <sup>14</sup>R. G. Kleva and J. F. Drake, *Phys. Fluids* **27**, 1686 (1984).
- <sup>15</sup>W. Horton, *Plasma Phys. Controlled Fusion* **27**, 937 (1985).
- <sup>16</sup>H. W. Herrmann *et al.*, *Nucl. Fusion* **37**, 293 (1997).
- <sup>17</sup>I. S. Gradshteyn and I. M. Ryzhik, *Table of Integrals, Series, and Products*, 5th ed. (Academic, New York, 1994), Eq. (6.631).
- <sup>18</sup>B. Gabutti, "New asymptotics for the zeros of Whittaker's functions," *Numer. Algorithms* **28**, 159–170 (2001).
- <sup>19</sup>J. E. Howard and S. M. Hohns, *Phys. Rev. A* **29**, 418 (1984).
- <sup>20</sup>D. del-Castillo-Negrete, J. M. Greene, and P. J. Morrison, *Physica D* **91**, 1 (1996).
- <sup>21</sup>S. Shinohara and Y. Aizawa, *Prog. Theor. Phys.* **97**, 379 (1997).
- <sup>22</sup>M. V. Budyansky, M. Yu. Uleysky, and S. V. Prants, *Phys. Rev. E* **79**, 056215 (2009).